CFD Simulation of Flow Past Micro Air Vehicle Wings

Pradeep Shetty, M.B.Subrahmanya, D.S. Kulkarni, B.N.Rajani

NAL PD

Computational & Theoretical Fluid Dynamics Division
CSIR-National Aerospace Laboratories, Bangalore 560 017

February 2013

Contents

1 Introduction **1**

1.1 Background 1

1.2 Scope of the present work 2

1.3 Documentation outline 2

2 Mathematical Modelling of Flow Physics **3**

2.1 Introduction 3

2.2 Governing equations 3

2.3 Turbulence modelling 3

2.4 Numerical solution of finite volume equation 4

3 Results and Discussion **5**

3.1 Computational Details 5

3.2 Flow past Rectangular wing 6

3.3 Black Kite wing 7

3.4 Golden Hawk wing 10

3.5 Relative performance 18

4 Concluding Remarks **19**

1 Introduction

1.1 Background

Micro Air Vehicles (MAVs) are unmanned autonomous miniature flying machines which man has tried to mimic from the biological fliers like insects and small birds. A single MAV or a swarm of MAVs can be used effectively for surveillance so as to measure or gather relevant reliable information in hostile environments. These MAVs require the ability to loiter for a long duration and also have an efficient maneuver capability both in open and confined space. In many situations, MAVs can provide reliable solutions which are also extremely cost-effective. These MAVs usual have a maximal size of 30 cm and flight speed ranging between 12 to 14 m/s with 30 minute endurance and weighing below 300 g. Recently MAVs have gained interest and have been used for both military and civilian purpose. Two important challenging problems in design of MAVs are (i) low Reynolds number (Re) which results in unfavourable aerodynamic conditions to support controlled flight, and (ii) small physical dimensions, resulting in certain unfavourable scaling characteristics including structural strength, reduced stall speed, and low inertia. The small length and the low velocity resulting in a flight regime with a very low Reynolds number $(10^4 < Re < 5 \times 10^5)$ pose challenges in aerodynamic design of MAVs. The aerodynamics of wings and wing sections in this low Reynolds number regime is one of the interesting and less understood aspects of MAVs. Several factors which contributed to this poor performance are lack of understanding of aerodynamics, structural mechanics and the propulsion system at the micro scale and also the inadequate knowledge on the visual guidance and navigation systems.

Aerodynamic design of MAVs, reported so far, have employed different kinds of efficient lift generation systems viz., fixed wing [1, 2, 3], flapping wings [4, 3] , flexible wing [5] and rotary wings [6] and or their combinations. The fixed-wing MAVs are commonly used because they are simple and easy to implement and they usually fly at the upper end of the low Reynolds number regime $(Re > 1 \times 10^5)$ [7, 8]. It is well known from literature [7, 9]. that at low Reynolds number, the aerodynamic characteristics greatly depend on the wing geometry. In general the MAVs require aerofoil with small thickness and significant camber in order to have a better aerodynamic performance at low Reynolds number. Furthermore the small dimension of MAV demand wing with low aspect ratio. Literature [1, 2, 3] shows that wing planforms which are rectangular, elliptical, circular or its variants are ideal for MAV application since they offer more lifting area. National Aerospace Laboratories (CSIR) and Aeronautical Development Establishment (DRDO) have initiated a joint effort to design and develop fixed wing MAVs under the National Programme for Micro Air Vehicle (NP-MICAV) and eventually demonstrate the technology developed as a flying unit with pre-defined mission. As a part of this project, turbulent flow analysis past low aspect ratio (AR) thin wings have been carried out using the in-house code 3D-PURLES to study their relative aerodynamic performance at low Reynolds number.

1.2 Scope of the present work

The current work mainly focuses on the three-dimensional numerical simulation of turbulent flow past three low aspect ratio wings typical used for MAV application. The relative performance of these wing at low Re has been analysed by comparing the variation of lift, drag and moment coefficients. Aerodynamic coefficients obtained from the present simulation have also been compared with the available measurement data. These 3D analysis have been carried out using the in-house multiblock structured flow solution code 3D-PURLES [10, 11, 12, 13] This in-house code is based on an implicit finite volume algorithm to solve the time-averaged Navier Stokes equations for unsteady incompressible turbulent flow.

1.3 Documentation outline

The present document consists of four sections starting with this intoduction as the first one. The mathematical modelling of equations of turbulent fluid motion is described in Section 2. Results on turbulent flow past different wings for different flow Reynolds numbers at different angles of attack are discussed in Section 3, followed by few important concluding remarks and the scope of future work in Section 4.

2 Mathematical Modelling of Flow Physics

2.1 Introduction

The three-dimensional unsteady flow analysis around wing sections at different Re numbers has been carried out through numerical solution of the relevant Navier Stokes (NS) equation system. The numerical simulation of the NS equation needs an appropriate mathematical model which can handle the geometrical complexities like arbitrary shaped boundaries as well as the physical complexities like simulating the effects of turbulence.

2.2 Governing equations

The phase-averaged Navier Stokes equation for unsteady turbulent incompressible flow in the *non-orthogonal curvilinear coordinates* with cartesian velocities as dependent variables is written in a compact form as follows:

Momentum transport for the Cartesian velocity component $\langle U_i \rangle$:

$$\frac{\partial}{\partial t}\left(\rho\langle U_i\rangle\right) + \frac{1}{J}\frac{\partial}{\partial x_j}\left[\rho\langle U_i\rangle\langle U_k\rangle\beta_k^j + \langle P\rangle\beta_i^j - \frac{\mu}{J}\left(\frac{\partial\langle U_i\rangle}{\partial x_m}B_m^j + \frac{\partial\langle U_k\rangle}{\partial x_m}\beta_i^m\beta_k^j\right) - \rho\langle u_i u_j\rangle\beta_k^j\right] = S_{U_i} \tag{2.1}$$

where, $\langle P\rangle$ and $\langle U_i\rangle$ are the phase-averaged pressure and velocity components along i direction respectively. μ is the fluid viscosity, B_k^j and b_k^j are the metric coefficients due to transformation from cartesian to curvilinear coordinates and J is the Jacobian of the transformation matrix. u_i is the fluctuating velocity components and S_{U_i} is any momentum source other than the pressure gradient These momentum equations are further supplemented by the mass conservation (continuity equation).

Mass Conservation (Continuity):

$$\frac{\partial}{\partial x_j}\left(\rho\langle U_k\rangle\beta_k^j\right) = 0 \tag{2.2}$$

However Eq. 2.1 and Eq. 2.2 do not form a closed system due to the presence of the unknown turbulent stress term $-\rho\langle u_i u_j\rangle$.

2.3 Turbulence modelling

In Eddy Viscosity based turbulence models, the turbulent stress appearing in the Reynolds-Averaged equations is expressed in terms of the mean velocity gradients as following:

$$-\rho\langle u_i u_j\rangle = \mu_t\left(\frac{\partial\langle U_i\rangle}{\partial x_j}+\frac{\partial\langle U_j\rangle}{\partial x_i}\right)-\frac{1}{3}\rho\delta_{ij}\langle u_m u_m\rangle \tag{2.3}$$

where, δ_{ij} is the Kronecker Delta and *m* is the summing index over $m = 1, 2, 3$. The term $\frac{2}{3}\rho k\delta_{ij}$ ensures that the sum of the normal stresses is *2k* as per definition of the turbulence kinetic energy ($k = \frac{1}{2}\overline{u_i u_j}$). The eddy viscosity μ_t is assumed to be an isotropic scalar quantity whose value depends on the local state of turbulence. Three different turbulence models used in the present work are the standard $k-\epsilon$ model [14], Shear Stress Transport (SST) model proposed by Menter [15] and one equation model of Spalart-Allamaras (SA) [16]. The details of all these turbulence models are discussed in the report [12].

2.4 Numerical solution of finite volume equation

3D-PURLES is a finite volume procedure for numerical solution of Navier Stokes equation using collocated variable arrangement in non-orthogonal curvilinear coordinates. The algorithm uses either upwind scheme or higher order low diffusive schemes (CDS, QUICK, 2^{nd} order upwind) for discretisation of spatial derivatives in the convective fluxes and second order accurate three-level fully implicit scheme for the temporal derivatives. Using the relevant geometric factors, appropriate discretisation schemes and linearisation of the source vector $\langle S\rangle$, the transport of momentum components or turbulence scalars are expressed in the following form of flux balance equation

$$\left(1.5\phi_p^{n+1}+0.5\phi_p^{n-1}-2\phi_p^n\right)\frac{\Delta V}{\Delta t}=\sum_{nb}A_{nb}\phi_p^{n+1}+SU-A_P\phi_P^{n+1} \tag{2.4}$$

where $A_P = \sum_{nb} A_{nb} - SP$; the coefficient A_{nb} represents the combined effect of convection and diffusion at the six faces of a computational cell denoted by the suffix *nb*; *SU* and *SP* are the components of the linearised source term $\langle S\rangle$, ΔV is the cell volume and Δt is the time step size. The scalar ϕ represents the velocity components in general and also the turbulence scalars used in the URANS computations. The superscripts of ϕ represent the respective time step. The continuity equation is also transformed to a linearised equation for pressure correction in the form of Eq. 2.4 and the corrections for pressure and velocity field obtained are added to the momentum-satisfying pressure and velocities respectively at the cell centers and cell faces. The detailed derivation of Eq. 2.4 and the iterative decoupled approach to handle the pressure-velocity link are reported elsewhere [17, 11]. The system of linearised equations (Eq. 2.4) for velocity, pressure and turbulence scalars are solved using the strongly implicit procedure of Stone [18]. For the turbulent flow situations, turbulence is modelled either by using the URANS [12] or LES methodology [13]. The algorithm is also successfully parallelized for cost effective computation on multiple processors using standard MPI routines.

3 Results and Discussion

Three dimensional flow simulation has been carried out using the in-house flow code 3D-PURLES for three different wing configurations used in MAV's (1) Rectangular wing having a cross-section of Selig-4083 cambered plate with 1% thickness and semispan=$0.6C$ (where C is the length of the root chord) (2) Black Kite wing having a modified inverse Zimmerman planform whose cross-section is Selig-4083 cambered plate with 1% thickness and semispan=$0.6C$ (3) Golden Hawk having a modified cropped delta wing whose cross-section is modified Eppler-61 volumetric aerofoil and semispan=$0.625C$

3.1 Computational Details

The simulations have been carried out using the H-H grid topology since grid generation and prescription of flow boundary conditions are simple and straight forward. Similar grid topology has been used by Hsiao and Pauley [19] for simulating flow past rectangular wing.

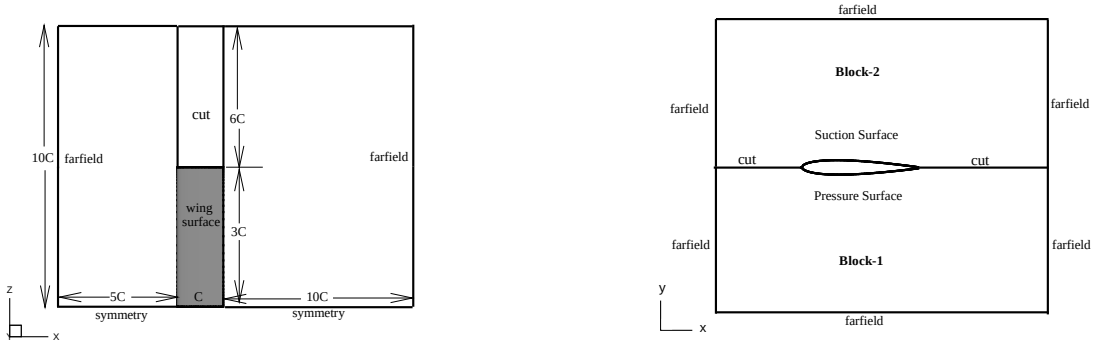

(a) Typical boundary conditions on X-Z plane

(b) Typical boundary conditions on X-Y plane

Figure 3.1: Boundary conditions and computational domain used for H-H grid topology

The present H-H grid topology consists of two blocks one covering the pressure side and other covering the suction side and have $193 \times 63 \times 69$ grid points in each block. The quasi 3D grids are generated by stacking 2D curvilinear grids [20] at each wing section along the span direction. The wing tip is closed linearly to obtain zero thickness. The present simulations have been carried out assuming the flow to be fully turbulent where the effect of turbulence is modelled using the standard $k - \epsilon$ model [14] and the upwind scheme has been used for the convective flux discretization. However for the Golden Hawk wing simulations, SA [16] and SST [15] turbulence models are also used in order to study the influence of the models in predicting the aerodynamic coefficients. The computational do-

main and the boundary conditions used for the present simulation are shown in Fig. 3.1. Depending on the sign of the convective flux on the relevant face, the farfield boundary condition is either treated as an inflow boundary where an uniform flow is prescribed or an outflow boundary condition where the normal gradients of the flow variables are made zero. At the wing surface wall nodes, no slip condition ($U = 0$, $V = 0$ and $W = 0$) is specified. At the block (cut) boundary, one overlap control volume is provided on the either side of the block interface boundary for appropriate transfer of the solution from the neighbouring block. The near wall boundary conditions for the turbulence scalars (k, ϵ, ω and $\tilde{\nu}_t$) have been appropriately used depending on the turbulence model chosen. The level of freestream turbulence kinetic energy (k) is maintained at 1% of the mean kinetic energy of the freestream whereas the value of the turbulence energy dissipation (ϵ) and the specific dissipation rate (ω) value at the inflow boundary nodes is prescribed assuming the local eddy viscosity (μ_t) to be approximately equal to ten times laminar viscosity (μ) for $k - \epsilon$ model and equal to laminar viscosity of SST model. For the SA turbulence model the value $\tilde{\nu}$ at the inflow boundary nodes are assumed to be equal to the laminar kinematic viscosity (μ/ρ). The surface grids for the Black Kite and Golden Hawk wings are shown in Fig.3.2. The grids are generated so as to maintain a near wall y^+ ranging between 11 to 30 as required for the standard $k - \epsilon$ model.

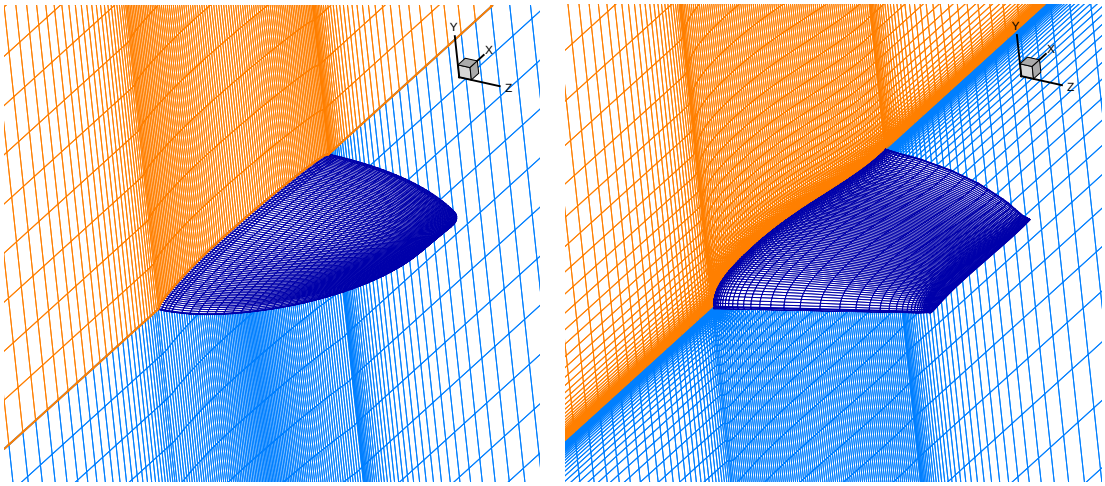

(a) Black Kite wing (b) Golden Hawk wing

Figure 3.2: Typical view of the grid showing the symmetry plane and the wing surface

3.2 Flow past Rectangular wing

The flow simulation over the rectangular wing at different angles of attack ranging between -8° to 34° has been carried out at $Re = 2.4 \times 10^5$ based on the root chord length (C) and a wind speed of 14 m/s. These flow conditions used are similar to that used for the Black Kite wing configuration and geometrically the rectangular wing differs from Black Kite wing only in the shape of the planform. Torres and Mueller [7] measurement results are available for similar Selig rectangular wing planform at slightly different flow conditions. The experiments were carried out for rectangular wing having a

semi-span of $0.5C$ at $Re = 10^5$. The computational results obtained using first order upwind scheme have been compared with the measurement data of Torres and Mueller [7]. This simulation was basically carried out as part of the confidence building exercise of 3D-PURLES code to handle thin wings at low Re configurations.

The aerodynamic coefficient computed from the present simulation is observed to match reasonably well with the measurements as shown in the Fig. 3.3. In both measurement and computation, the stall is observed to be very mild unlike the sharp stall observed in traditional wings with large aspect ratio. The stall angle ($\alpha \approx 29^\circ$) and maximum lift obtained from the present computation is lesser than the measurement value ($\alpha \approx 40^\circ$). The discrepancies may be mainly attributed to the difference in the span length, Reynolds number and root section used in the experiments. The present simulation assuming the flow to be fully turbulent could capture the non-linearity observed in the measurement data lower positive angles. This difference in the lift coefficient may also be primarily attributed to the inability of the present simulation to handle transitional flows. The non-linearity of the lift curve is usually observed in measurements carried out at low Reynolds number($Re \leq 10^5$) for both wings [7] and wing sections [21] This non-linearity at lower angles of attack is a typical characteristics of low Reynolds number flows which may be primarily attributed to the fact that the flow under goes transition from laminar to fully turbulent flow as the angle of attack increases. Some preliminary two-dimensional simulations carried out at $Re = 60000$ for Eppler-387 using 3D-PURLES by fixing transition location in available turbulence models gave some promising results [22] However the value and location of maximum L/D computed from the present simulation is found to be in good agreement with the measurement value.

The surface pressure contours and cross-flow pattern obtained at three different angles of attack ($\alpha = 4^\circ$, 20° and 30° are shown in Fig. 3.4. The cross flow patterns clearly show the signature of the tip vortex up to $X/D = 1.5$. Fig. 3.5 shows the particle traces obtained at three angles of attack which clearly shows the formation of the tip vortex.

3.3 Black Kite wing

Flow analysis past Black Kite wing has been carried out for 14 m/s wind speed ($Re = 2.4 \times 10^5$) based on the initial discussion with the MAV team. However the NAL Experiments were carried out at 12 m/s ($Re = 2.057 \times 10^5$) and in order to study the effect of wind speed, simulations have also been carried out at 12 m/s at few typical angles of attack. The effect of wind speed as shown in Fig. 3.6 clearly indicates an insignificant difference in the aerodynamic coefficients obtained for these two speeds. This trend obtained at 12 m/s and 14 m/s were observed in NAL experiments [23] as well. Based on this comparative study, the aerodynamic coefficients obtained by the 14m/s simulations are compared with the NAL wind tunnel measurement data [23] for the full configuration (fuselage + wing + tail) and shown in Figure 3.7. The lift coefficient (C_l) and the drag coefficient (C_d) computed along the flow axis from the present simulation (Fig. 3.7(a) and Fig. 3.7(b)) is observed to agree reasonably well with the measurement data for the lower range of angles of attack ($\alpha < 15^\circ$).

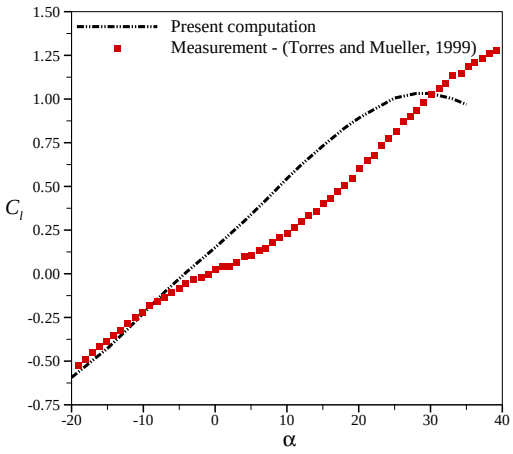

(a) Coefficient of lift

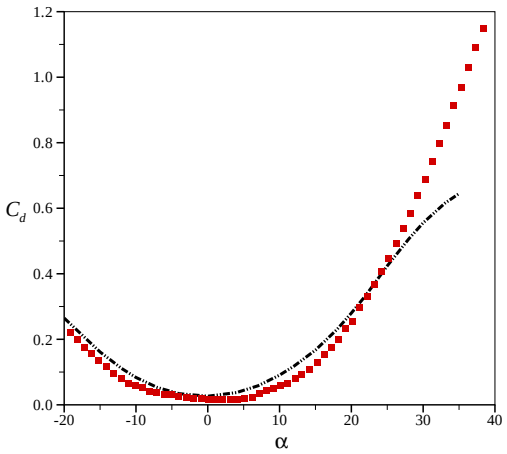

(b) Coefficient of drag

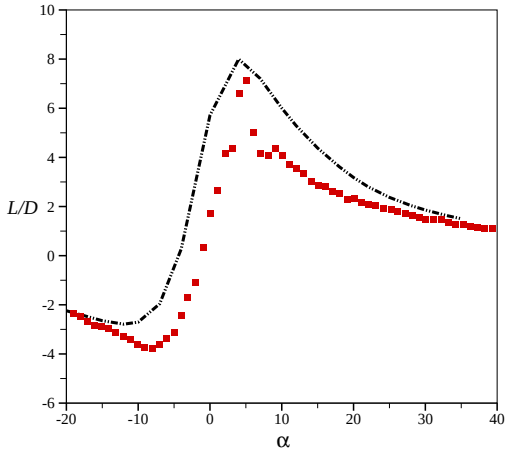

(c) Lift to drag ratio

Figure 3.3: Variation of aerodynamic coefficients for flow past rectangular wing

A small kink (slope discontinuity) is observed in the C_l curve for 14 m/s simulation which is also reported by Mueller in his experiments for low Re wing configurations [7]. The present simulation has predicted a soft stall at about 35° angle of attack which is typical of low Reynolds number wing as observed in Torres and Mueller experiments [7] carried out for low aspect ratio wings at low Reynolds number. The stall angle and nature of stall can not be compared with the NAL experiments due to the nonavailability of measurement data beyond $\alpha = 24^\circ$ where C_l is observed to be still in the increasing trend. Figure 3.7(d) clearly shows that the 3D-PURLES has predicted a higher maximum lift-to- drag ratio when compared to the experiments. The location of maximum L/D obtained by the present simulation is about $(\alpha = 4^\circ)$ which is slightly underpredicted when compared to the measurement $(\alpha = 7^\circ)$. The computed pitching moment (C_m) about the leading edge of the wing (Fig. 3.7(c)) is observed to agree well with the measurement data at lower angles of attack. At higher angles of attack the present simulation has captured the trend but with a different slope when compared to the

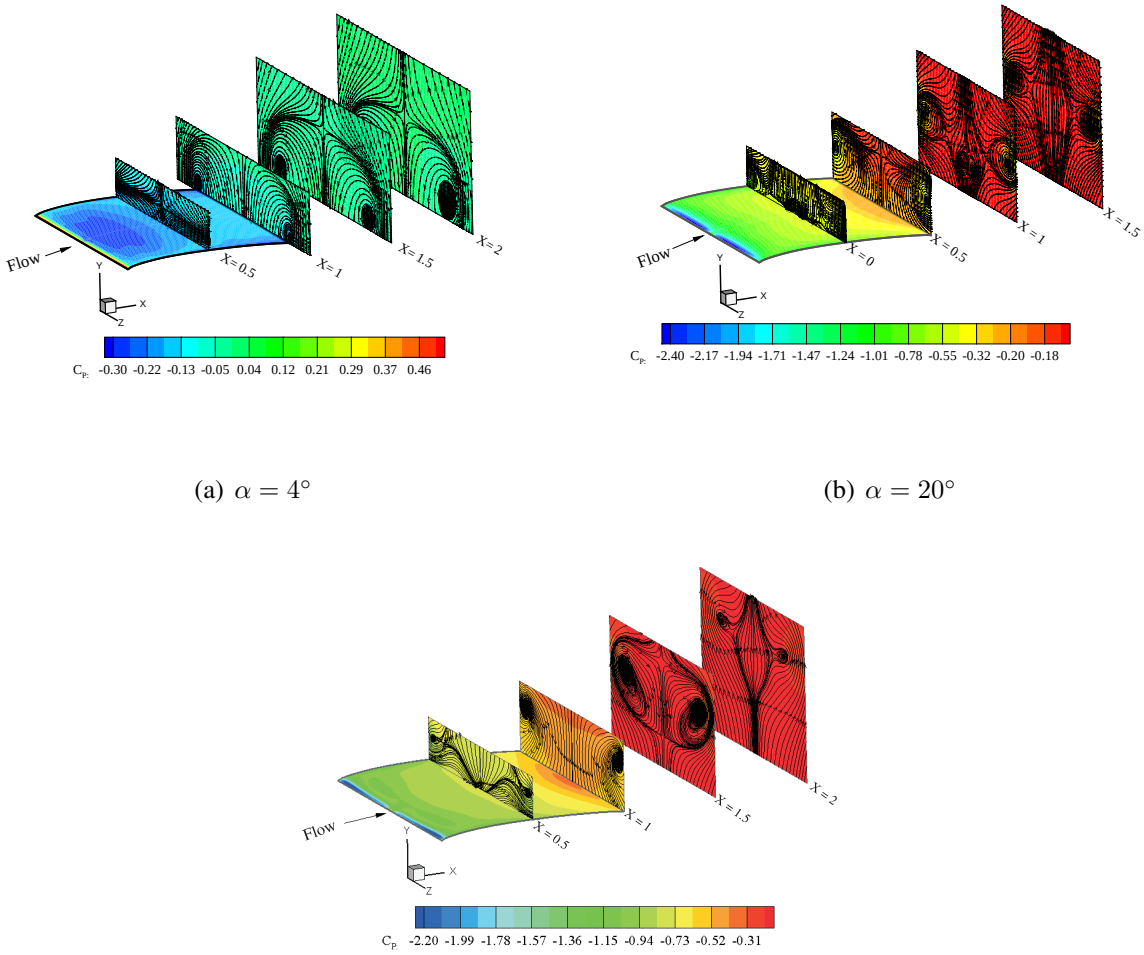

(a) $\alpha = 4°$

(b) $\alpha = 20°$

(c) $\alpha = 30°$

Figure 3.4: Surface pressure contours and cross-flow pattern for rectangular wing ($Re = 2.4 \times 10^5$)

measurement. The discrepancies observed at higher angles of attack may be due to the influence of the fuselage and the tail which has not been considered for the present simulation. However the experiments indicate that the presence of the tail has an insignificant effect on the aerodynamic performance of the Black Kite configuration. In addition, on the computation side, this discrepancy may also be due to the inadequate grid resolution, lower order discretization scheme and inability to model the transition. On the other hand the accuracy of the present experimental data is not clearly quantified as the error band and conditions used has not been specified.

The non- dimensionalised pressure contours on the wing surface with the cross-flow patterns up to a length of $1.5C$ in the wake are shown in the Fig. 3.8 at three different angles of attack. The pressure distribution obtained is quite realistic with the reduction in suction pressure as the angle of attack increases. The cross-flow pattern clearly indicates the complex vortex generated due to the flow past a finite wing which is observed to be more prominent at higher angles of attack.

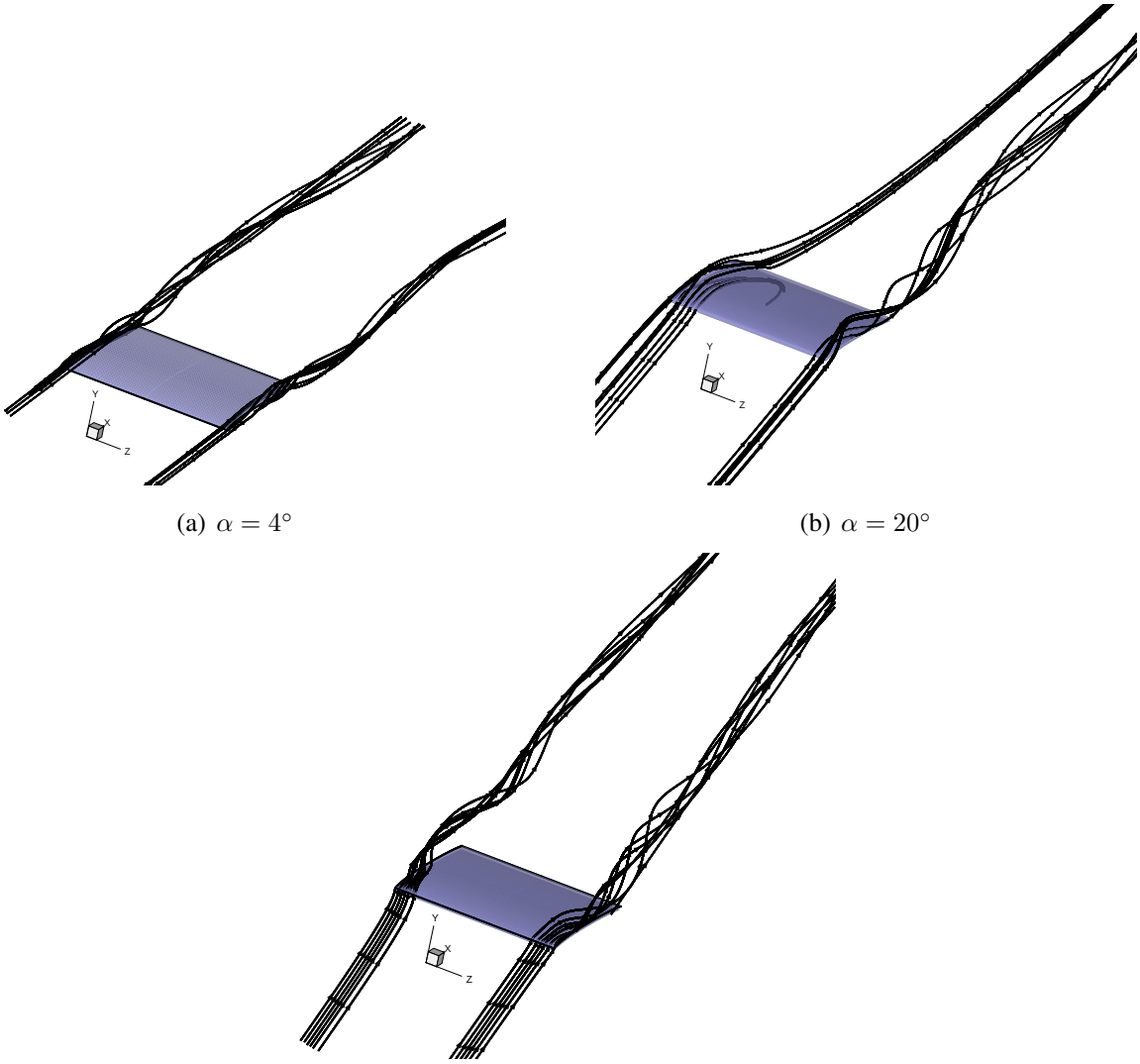

(a) $\alpha = 4°$

(b) $\alpha = 20°$

(c) $\alpha = 30°$

Figure 3.5: Particle trace for rectangular wing showing the tip vortex ($Re = 2.4 \times 10^5$)

Figure 3.9 shows the particle trace typically at three angles of attack ($\alpha = 4°$, $20°$ and $30°$). The formation of the tip vortex is clearly evident especially at higher angles of attack. The wing tip vortices are caused due to the pressure difference between the upper surface (low pressure) and lower surface (high pressure) of the wing. This tip vortex induces a circulatory motion over the wing tip which affects the wing aerodynamics. In the downstream of the wing these tip vortices cause a secondary motion resulting in the formation of the wake vortex.

3.4 Golden Hawk wing

The aerodynamic coefficients for the Golden Hawk wing obtained from the present simulation at 12m/sec wind speed ($Re = 1.7 \times 10^5$) using three different turbulence models are compared with the NAL wind tunnel measurement data [23] for the Golden Hawk full configuration (fuselage +

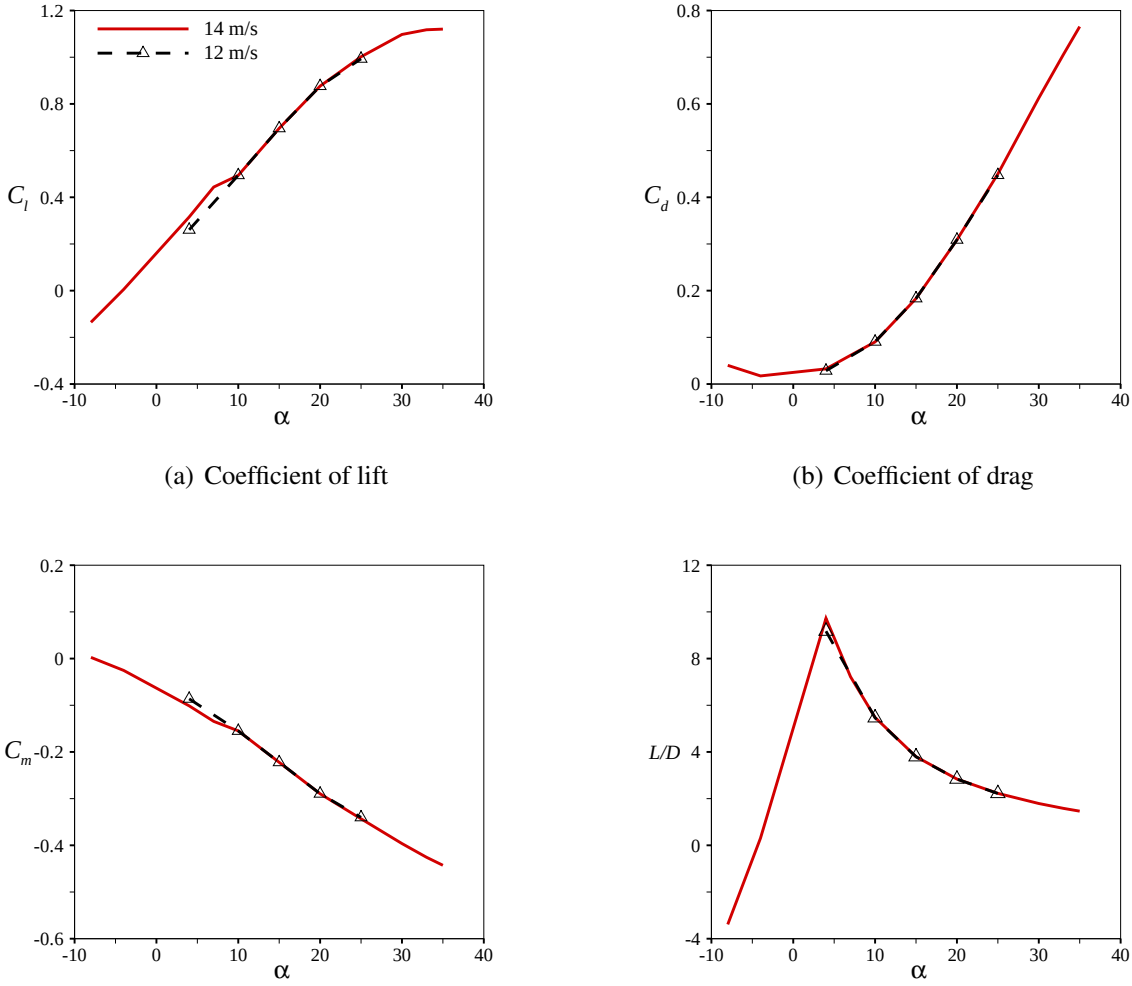

(a) Coefficient of lift

(b) Coefficient of drag

(c) Coefficient of moment

(d) Lift to drag ratio

Figure 3.6: Variation of aerodynamic coefficients for flow past Black Kite wing

wing + winglet) and also for the configuration without winglet (fuselage + wing) and are shown in Fig. 3.10. The NAL experiments show that the presence of winglet has slightly enhanced the lift and drag coefficient but reduces the stall angle. The computed coefficient of lift (Fig. 3.10(a)) agrees reasonably well with experimental data up to $\alpha \approx 20^\circ$ where the MAV configuration without winglet is observed to stall experimentally. All the three turbulence models have predicted almost identical C_l for α ranging between -8° to 26°. Beyond 26° the SA and SST models have predicted higher C_l when compared to the standard $k - \epsilon$ model. Further the measurement predicted a very early stall (α between 16° and 17° for full configuration and α between 18° and 20° for without winglet configuration) whereas the present computation has predicted the stall angle between 34° and 36°. This early stall behaviour of the Golden Hawk wing contradicts the Black Kite wing where the NAL measurement does not indicate the stall even up to $\alpha = 25^\circ$. The measurements carried out by Torress and Mueller [7] for different wing planforms (rectangular, Zimmerman, inverse Zimmerman and elliptical) for 0.5 aspect ratio shows that the stall occurs beyond $\alpha = 35^\circ$. It was communicated

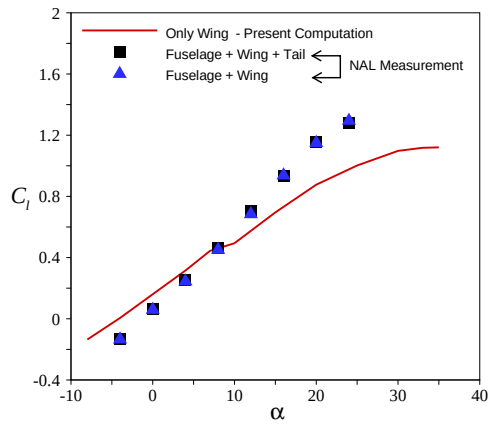

(a) Coefficient of lift

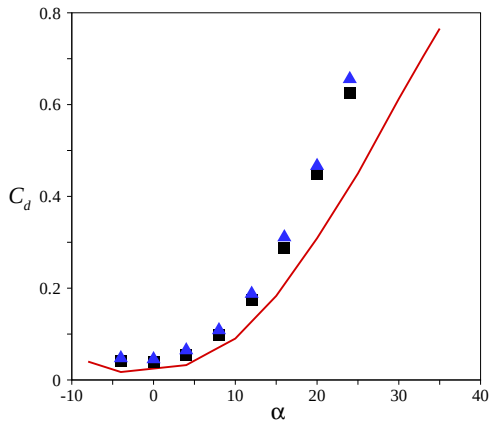

(b) Coefficient of drag

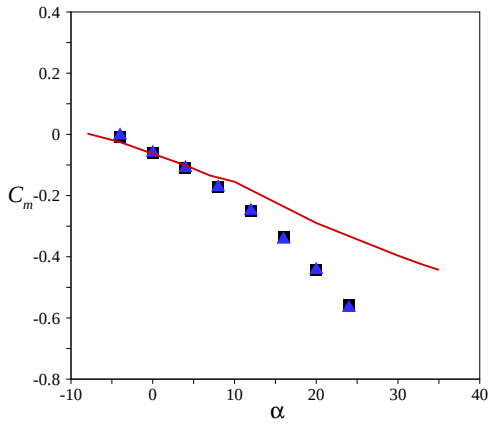

(c) Coefficient of moment

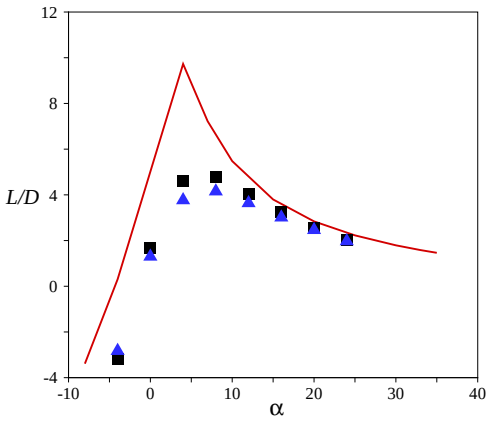

(d) Lift to drag ratio

Figure 3.7: Variation of aerodynamic coefficients for flow past Black Kite wing

to us orally by the design team that this early stall was not observed even during the flight test carried out for the Golden Hawk configuration. However the computation has predicted almost the same stall angle for both the configurations. Similar to the lift component the computed drag coefficient (Fig. 3.10(b)) matches well with the measurement data up to $\alpha \approx 20^{\circ}$. The C_d predicted by all the three models almost coincide with one another up to $\alpha = 26^{\circ}$ beyond which the SA and SST have predicted a higher drag when compared to the standard $k - \epsilon$ model. The lift-to- drag ratio (L/D) obtained by the present simulation (Fig. 3.10(d)) using the standard $k - \epsilon$ model and SST matches fairly well with measurement data for the whole range of α with the maximum $L/D(= 7.6)$ over predicted as compared to measurement $(L/D = 5.93)$. On the other hand, the SA model has grossly over predicted the maximum $L/D(= 11.3)$ but the location at which the maximum L/D occurs is same for all the three models $(\alpha = 4^{\circ})$ which is slightly earlier than the measurement value $(\alpha = 6^{\circ})$. However the coefficient of moment (Fig. 3.10(c)) obtained from the present simulation using three different turbulence models is found to match well with the measurement data. The C_m obtained

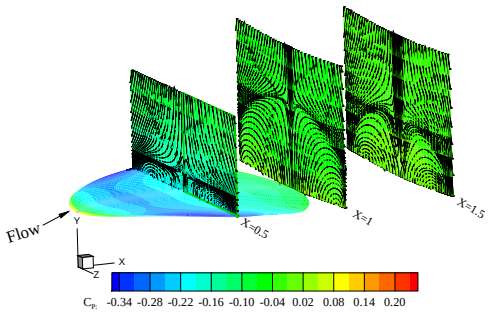

(a) $\alpha = 4°$

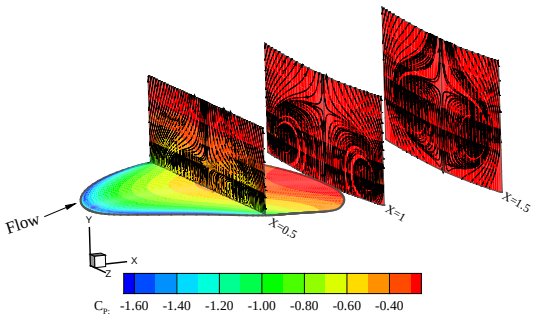

(b) $\alpha = 20°$

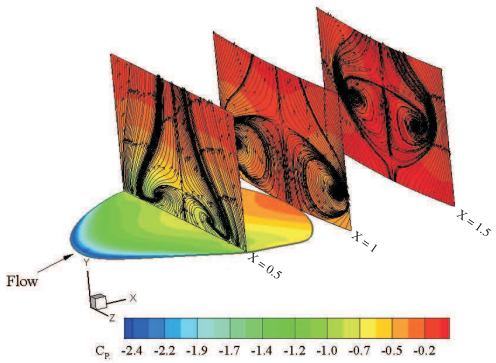

(c) $\alpha = 30°$

Figure 3.8: Surface pressure contours and cross-flow pattern for Black Kite wing ($Re = 2.4 \times 10^5$)

experimentally shows a kink in the curve at the stall angle which is not seen in the computations. The discrepancies observed may be primarily attributed to the fact that the simulations have been carried out only for the wing configuration whereas the experiments have been carried out for the full configuration. On the computation side, more detailed analyses needs to be carried out by refining the grid size and using a different grid topology and also higher order discretisation scheme. Modelling the effect of transition which plays a prominent role at the low Reynolds number flows may improve the computational results. In order to justify the accuracy of the present computation, the comparison with the experiments for only the wing configuration would be more appropriate and due to lack of the measurement data this comparison exercise could not be carried out.

The non-dimensionalised pressure contours on the wing surface with the cross-flow patterns up to a length of $1.5C$ in the wake are shown in the Fig. 3.11 at three different angles of attack. Similar to Black-kite wing the signature of the tip vortex has been captured reasonably well with its strength increasing with angle of attack. However, the vortex is observed to diffuse at the downstream stations.

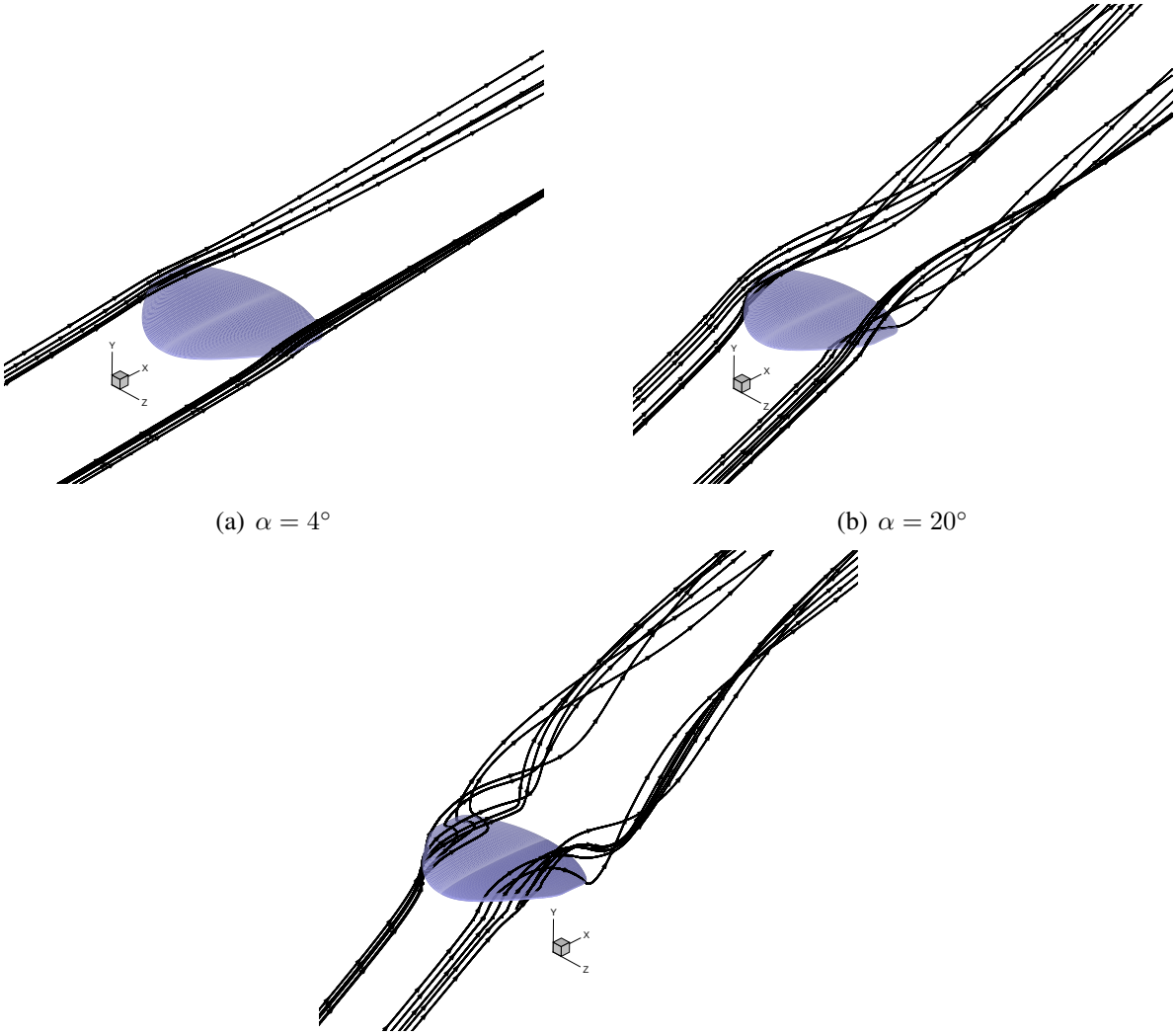

(a) $\alpha = 4°$

(b) $\alpha = 20°$

(c) $\alpha = 30°$

Figure 3.9: Particle trace for Black Kite wing showing the tip vortex ($Re = 2.4 \times 10^5$)

The diffusion of the vortex may be due to the coarse grid resolution in the wake and the upwind scheme used in this simulation. The use of higher order scheme which is less diffusive compared the upwind scheme is likely to improve the cross flow pattern. In the present simulation the higher order scheme had convergence issues which is being looked into. The present simulation has captured the tip vortex for the Golden Hawk wing reasonably well as shown in Figure 3.12.

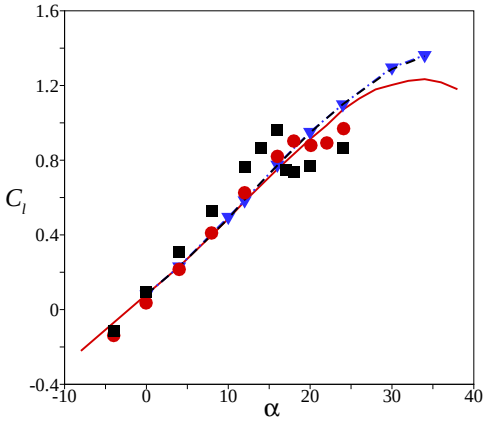

(a) Coefficient of lift

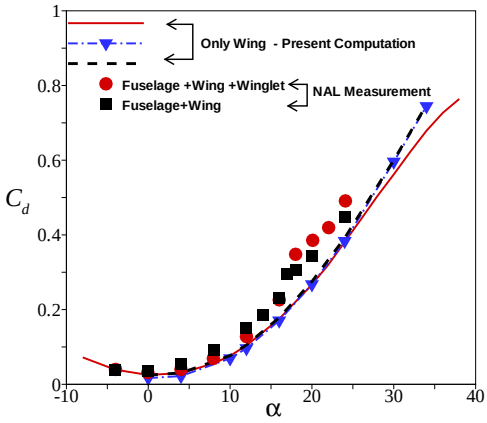

(b) Coefficient of drag

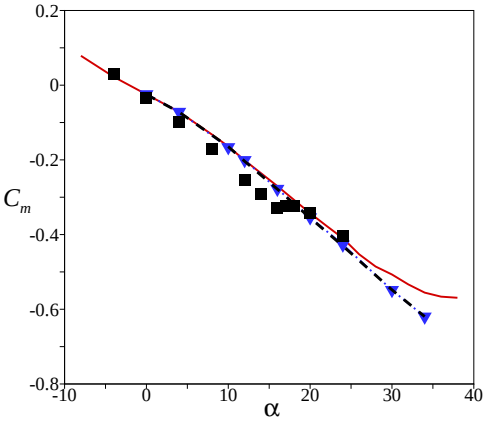

(c) Coefficient of moment

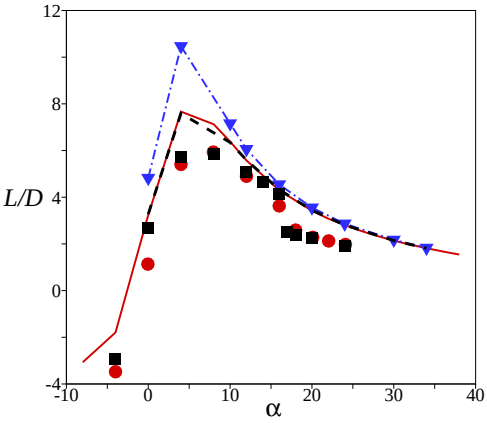

(d) Lift to drag ratio

Figure 3.10: Variation of aerodynamic coefficients for flow past Golden Hawk wing

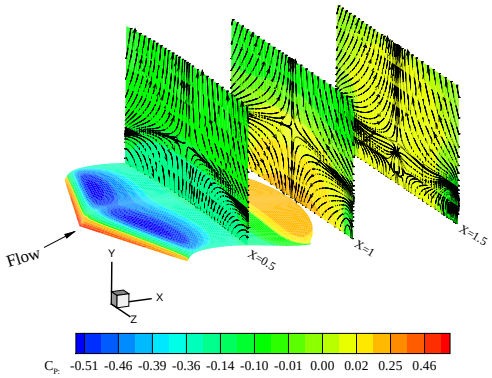

(a) $\alpha = 4°$

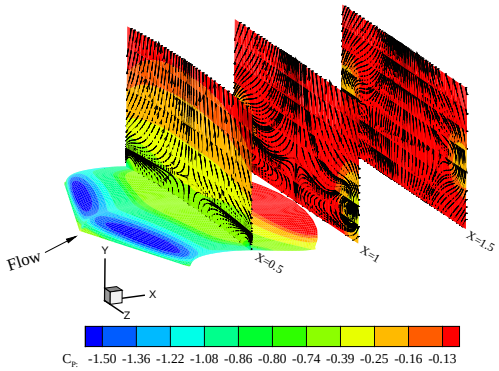

(b) $\alpha = 20°$

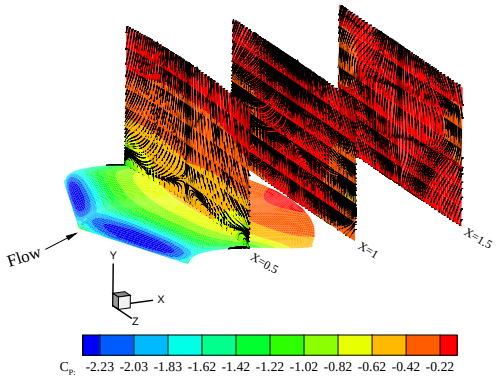

(c) $\alpha = 30°$

Figure 3.11: Surface pressure contours and cross-flow pattern for Golden Hawk wing ($Re = 1.7 \times 10^5$)

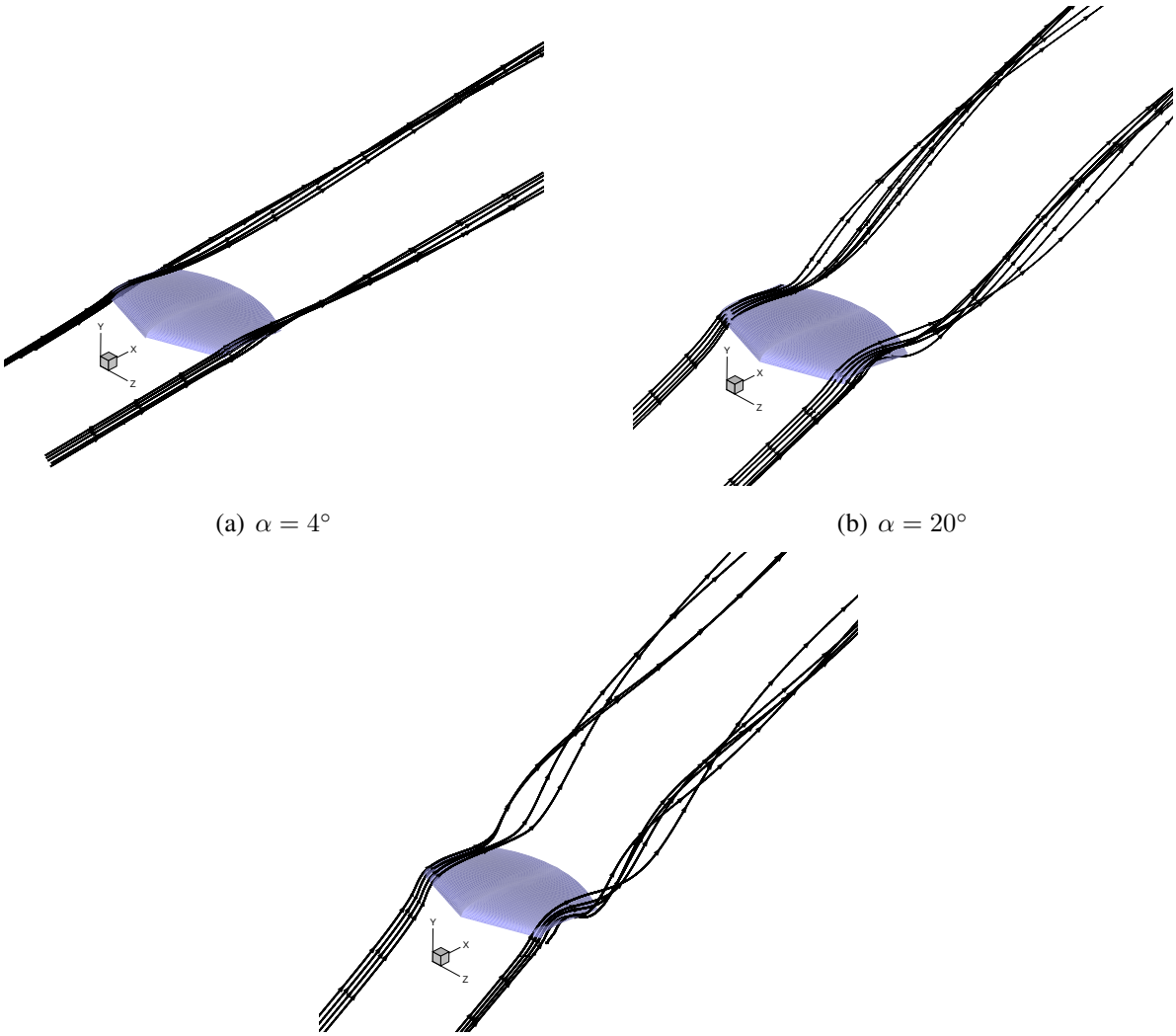

(a) $\alpha = 4°$

(b) $\alpha = 20°$

(c) $\alpha = 30°$

Figure 3.12: Particle trace for Golden Hawk wing showing the tip vortex ($Re = 1.7 \times 10^5$)

3.5 Relative performance

The relative performance of the three wings is shown in Fig. 3.13. The variation of the aerodynamic forces obtained for the three wings is observed to follow a similar trend. Figure 3.13(a) clearly shows that the rectangular and Black Kite wing have higher lift at the lower angles of attack whereas the Golden Hawk wing has a higher lift near the stall angle. The present computation indicates that the stall for both the Golden Hawk wing and the Black Kite wing occurs almost at the same angle of attack whereas rectangular wing stalls earlier. The variation of the drag coefficient (Fig. 3.13(b)) for the three wings does not differ significantly. The C_d computed for the Black Kite is observed to be slightly higher beyond $\alpha = 15°$. The location of the maximum L/D (Fig. 3.13(d)) for all the three wings is obtained at the same angle of attack ($\alpha = 4°$) with the Black Kite having the maximum L/D. The comparison of the variation of the C_m (Fig. 3.13(c)) clearly indicates that the Golden Hawk wing has a better stability.

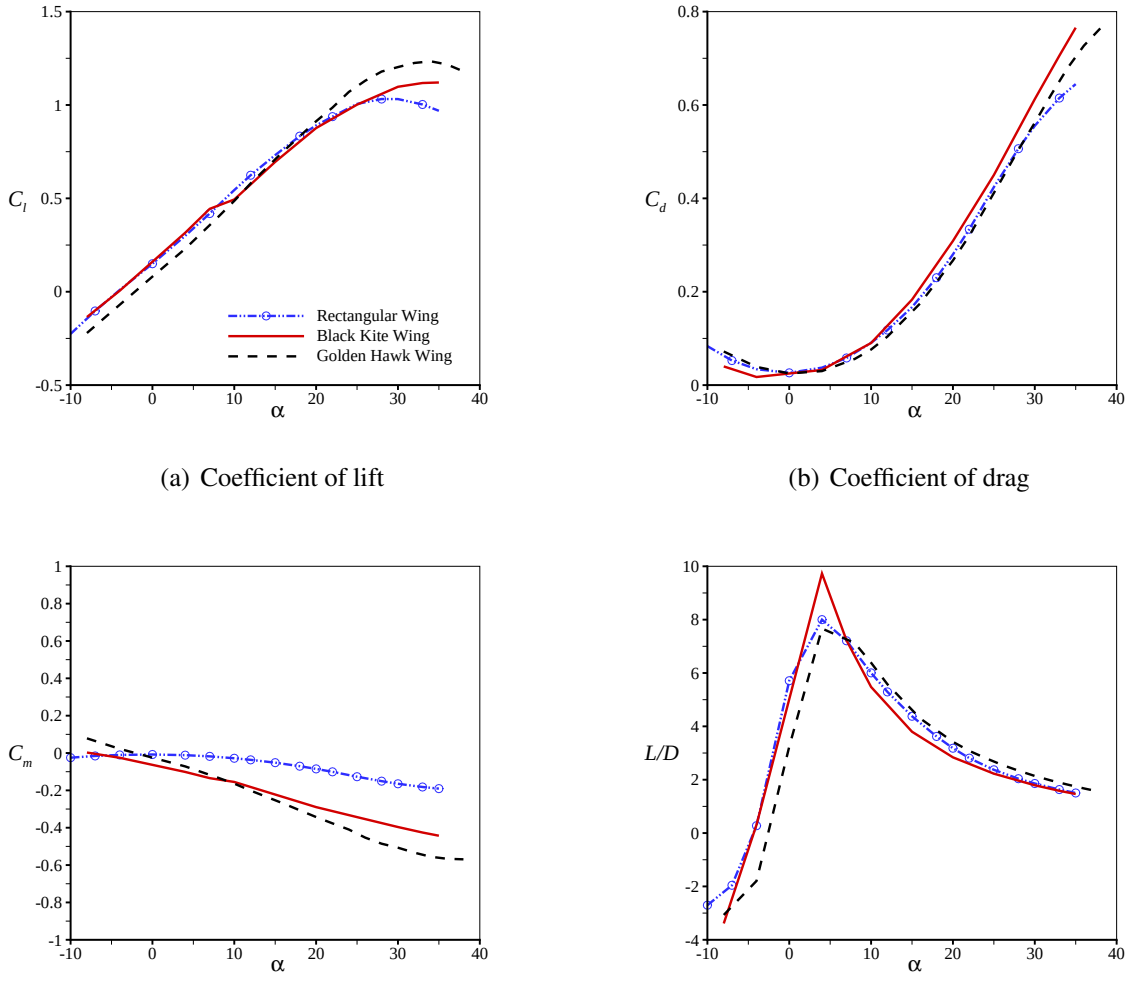

(a) Coefficient of lift

(b) Coefficient of drag

(c) Coefficient of moment

(d) Lift to drag ratio

Figure 3.13: Relative performance of three wings

4 Concluding Remarks

The 3D-PURLES flow solution code has been used successfully to predict the aerodynamic characteristics of MAV wings at low Reynolds number. The present simulation carried out for the rectangular wing matches the measurement in qualitative sense. The nature of the stall and the maximum L/D predicted by this simulation matches reasonably well with the measurement. The non-linear trend observed in the variation of C_l in the measurement has not been captured by this simulation. This discrepancy observed may be mainly because the present simulation has been carried out assuming the flow to be fully turbulent and not modelling the transition region. The rectangular wing simulation confirms the accuracy and adequacy of the present flow solution code to predict flow past finite wing with low aspect ratio. The present computation for the Black Kite wing is able to capture the trend of the aerodynamic coefficients obtained by NAL measurements reasonably well. The discrepancies may be due to the fact that NAL experiments were carried out for full configuration. For the Golden Hawk wing, the aerodynamic coefficients obtained by the present simulation matches well with the measurement data at lower angles of attack ($\alpha < 20^\circ$). The discrepancies observed at higher angles of attack may be mainly attributed to the early stall obtained by the measurements. The use of different turbulence models for the Golden Hawk wing shows an insignificant effect on the aerodynamic characteristics for α ranging between -8° to 26° with SA model over predicting the $(L/D)_{max}$ when compared to SST and $k-\epsilon$ model as well as the measurement data. No significant difference is observed in the variation of aerodynamic forces obtained by the three wings. The maximum lift to drag ratio obtained by Black Kite wing is 1.25 times higher than the golden hawk and rectangular wing. However the present computation indicates that the goldgen hawk is more stable. The present simulation has successfully captured the wake flow and tip vortex for all the three wings.

Work is in progress to incorporate appropriate transition modelling coupled to the eddy viscosity turbulence model in 3D-PURLES. The modelling of transition in the RANS framework is expected to give better estimate of the aerodynamic characteristics especially at this low Reynolds number flows. Efforts have been initiated to investigate the influence of grid refinement and grid topology on the computational results. The convergence issues faced due to the use of higher order scheme is being looked into.

Acknowledgments

The authors wish to express their heartfelt thanks to the Head CTFD Division, CSIR-NAL, Bangalore, for his support. We also deeply thank Head EAD Division, D. Arivoli Scientist and MAV team of the EAD Division, CSIR-NAL, Bangalore for sharing the experimental data.

References

[1] J. M. Grameyer and M. T. Keennon. Development of the black Mirco Air Vehicle. *AIAA Paper*, 2001-0127, 2001.

[2] T. J. Mueller. Aerodynamic measurement of low Reynolds number for fixed wing Micro-Air Vehicle. *VKI, Belgium, September 13-17*, 1999.

[3] T. J. Mueller, editor. *Fixed and Flapping wing aerodynamics for Micro Air Vehicle applications*, volume 195 of *Progress in astronautics and Aeronautics*, 1999.

[4] G. W. Jones, C. J. Bradshaw, J. Papadapoulos, and M. F. Paltzer. Improved performace and control of flapping-wing propelled Micro Air Vehicles. *AIAA Paper*, 2004-0399, 2004.

[5] W. Shyy, M. Berg, and D. Ljungqvist. Flapping and flexible wings for biological and micro vehicles. *Progress in Aerospace Sciences*, 35(5):455–506, 1999.

[6] B. R. Hein. Hover performance of a Micro Air Vehicle: Rotors at low Reynolds number. *AHS Lichten Award Competition*, 2005.

[7] G. E. Torres and T. J. Mueller. Aerodynamic characteristics of low aspect ratio wings at low reynolds number. In T. J. Mueller, editor, *Fixed and Flapping wing aerodynamics for Micro Air Vehicle applications*, volume 195 of *Progress in astronautics and Aeronautics*, pages 115–141. AIAA, 1999.

[8] M. S. Selig, J. J. Guglielmo, A. P. Broeren, and P. Giguere. Summary of Low-Speed Airfoil Data. *SoarTech Aero Publications, Virginia Beach*, 1, 1995.

[9] R. T. Jones. *Wing Theory*. Princeton University Press, 1990.

[10] S. Majumdar. Pressure based Navier Stokes solver for three-dimensional flow in hydrodynamics and low speed aerodynamics application . *Proc. 3^{rd} Asian CFD Conference, Bangalore*, 1:137–146, 1998.

[11] S. Majumdar, B. N. Rajani, D. S. Kulkarni, and M. B. Subrahmanya. Cfd simulation of low speed turbulent flow problems using unsteady rans and large eddy simulation approach. *Journal of Aerospace Sciences and Technologies*, 61:111–112, 2009.

[12] B. N. Rajani and S. Majumdar. Numerical simulation of turbulent flow past a circular cylinder. *NAL PD CF 0805*, 2008.

[13] B. N. Rajani and S. Majumdar. Large Eddy Simulation of flow past circular cylinder in the lower subcritical regime ($Re = 3900$). *NAL PD CF 1004*, 2010.

[14] B. E. Launder and D. B. Spalding. The numerical computation of turbulent flows. *Computer Methods and Applied Mechanics and Engg.*, 3:269, 1974.

[15] F. R. Menter. Two-equation eddy-viscosity turbulence models for engineering application . *AIAA J*, 32:269–289, 1994.

[16] P. R. Spalart and S. R. Allamaras. A one-equation turbulence model for aerodynamic flow. *AIAA paper*, 92-0439, 1992.

[17] S. Majumdar, W. Rodi, and J. Zhu. Three dimensional finite volume method for incompressible flows with complex boundaries. *Journal of Fluid Engineering, ASME*, :496–503, 1992.

[18] H. L. Stone. Iterative solution of implicit approximations of multidimensional partial differential equations. *SIAM Journal of Numerical Analysis*, 5:530–530, 1968.

[19] Chao Tsung Hsiao. and Laura L. Pauley. Numerical Study of the Steady State Tip Vortex Flow Over a Finite-Span Hydrofoil. *Journal of Fluids Engineering*, 120:345–353, 1998.

[20] A. Fathima, N. S. Baldawa, S. Pal, and S. Majumdar. Grid generation for arbitrary 2D configurations using a differential algebraic hybrid method . *NAL PD CF 9461*, 1994.

[21] M. S. Selig, C. A. Lyon, P. Gigure, C. N. Ninham, and J. Guglielmo. Summary of Low-Speed Airfoil Data. *SoarTech Publications, Virginia Beach*, 2, 1996.

[22] D. S. Kulkarni, M. B. Subrahmanya, and B. N. Rajani. Reliability of RANS Computations for Flow past an Aerofoil at Low Re. *4th Symposium on Applied Aerodynamics and Design of Aerospace Vehicle (SAROD 2009),Bangalore, India*, 2:630–640, 2009.

[23] D. Arivoli and Team. Pvt. Communication, EAD, CSIR-NAL, Bangalore.